PHYSICAL REVIEW E **89**, 053108 (2014)

Synchronization of particle motion induced by mode coupling in a two-dimensional plasma crystal

L. Couëdel,[1,*] S. Zhdanov,[2] V. Nosenko,[2,3] A. V. Ivlev,[2] H. M. Thomas,[2,3] and G. E. Morfill[2]

[1]*CNRS, Aix-Marseille Université, Laboratoire de Physique des Interactions Ioniques et Moléculaires, 13397 Marseille cedex 20, France*

[2]*Max Planck Institute for Extraterrestrial Physics, D-85741 Garching, Germany*

[3]*Forschungsgruppe Komplexe Plasmen, Deutsches Zentrum für Luft-und-Raumfahrt, Oberpfaffenhofen, Germany*

(Received 25 February 2014; published 30 May 2014)

The kinematics of dust particles during the early stage of mode-coupling induced melting of a two-dimensional plasma crystal is explored. It is found that the formation of the hybrid mode causes the particle vibrations to partially synchronize at the hybrid frequency. Phase- and frequency-locked hybrid particle motion in both vertical and horizontal directions (hybrid mode) is observed. The system self-organizes in a rhythmic pattern of alternating in-phase and antiphase oscillating chains of particles. The spatial orientation of the synchronization pattern correlates well with the directions of the maximal increment of the shear-free hybrid mode.

DOI: 10.1103/PhysRevE.89.053108 PACS number(s): 52.27.Lw

I. INTRODUCTION

An odd "kind of sympathy" in pendulum clocks discovered about 350 years ago by C. Huygens was later rigorously explained as a specific synchronization process between the weakly coupled close-frequency oscillators [1,2]. Since then synchronization phenomena have become an important topic in explorations of biological, physical, chemical, cybernetical, and many other dynamical systems. Their diversity and complexity required a principally new approach to develop a network analysis, allowing to systematically study intercorrelations in large populations of interacting units [3–8]. Spontaneous emergence of synchronized signals and spontaneous symmetry breaking are typical behaviors in such nonlinear systems, e.g., in spatially distributed mutually coupled lasers [9–11]. A large system of weakly coupled nearly identical oscillators with a phase-dependent interaction is normally considered as a model to explore collective synchronization in detail. Analytical studies [12], computational simulations [13], as well as model systems, e.g., the dynamics of disordered Josephson arrays [14], predict a nonlinear dynamical phase transition in such systems. In this sense, complex plasmas are ideal systems to observe the synchronization process generically in all its complexity and diversity at an "atomistic" scale and in real time.

Complex or dusty plasmas are weakly ionized gases containing micron-size particles called dust particles or microparticles. In a laboratory radio-frequency (rf) plasma these particles are negatively charged. Due to their strong interactions with the plasma and with each other, they can form strongly coupled systems, analogous to colloids [15]. Microparticles are often confined in the sheath region of electrical discharges, where the electrostatic force is strong enough to balance the gravity force. They can form monolayers or (quasi-)two-dimensional (2D) crystals [16–20] extended vertically to a finite width, which strongly depends on the strength of the vertical confinement [19]. In such systems, two in-plane wave modes with an acoustic dispersion can be sustained: a longitudinal mode and a transverse mode. Since the strength of the vertical confinement is finite, there is a third fundamental wave mode associated with the out-of-plane oscillations which has an optical dispersion [19–25].

Due to the strong electric field in the sheath region of the discharge, every particle is influenced by a strong ion flow exerting an additional force on it. Moreover, the screening cloud around each particle in such conditions is strongly distorted, being more extended in the direction of the flow. The ions tend to focus downstream of the particle making the system highly polarized. This mechanism is often referred to as "plasma wake" [26–33]. One of the easiest ways to represent the plasma wake is to add a pointlike positive wake charge downstream of the particle [23,25], or consider the polarization self-consistently in the framework of the linear response models [26,33–35].

The existing theories predict that all three wave modes depend critically on the parameters of the plasma wake. Moreover, the wake-mediated interactions between the particles result in the coupling of the "usual" crystal modes into a new "hybrid" mode of the lattice layer. This mode can be evidenced as localized "hot spots" in the lattice phonon's spectra [36]. The theory of mode-coupling instability [23,25,37] provides a detailed picture of a *plasma-specific* melting scenario operating in 2D plasma crystals. The melting associated with the wake-mediated coupling between the longitudinal in-plane and out-of-plane modes can only be triggered if (i) the modes intersect, and (ii) the neutral gas damping is sufficiently low. In the vicinity of the hybrid mode, one can observe traces of mixed polarization for the two intersecting wave branches [37]. These features can be considered as distinct fingerprints to identify the onset of the wake-induced mode coupling. In theoretical investigations [25,37] the hybrid mode was found to preferentially emerge with a wave vector parallel to the rows of the minimal packing density in the lattice. For instance, it is valid for the waves propagating at an angle $\theta = 0^\circ$ or along any other direction equivalent by hexagonal symmetry, e.g., at an angle $\theta = 60^\circ$ or 120°, etc. The propagation angle θ is as introduced in Fig. 1.

It is well known that in a system of coupled limit-cycle oscillators, a macroscopic fraction of them can synchronize to a common frequency when the coupling among oscillators is strong enough [38]. A two-dimensional plasma crystal can be seen as an ensemble of coupled nonlinear oscillators. During the mode-coupling induced melting, dust particles interact

*lenaic.couedel@univ-amu.fr

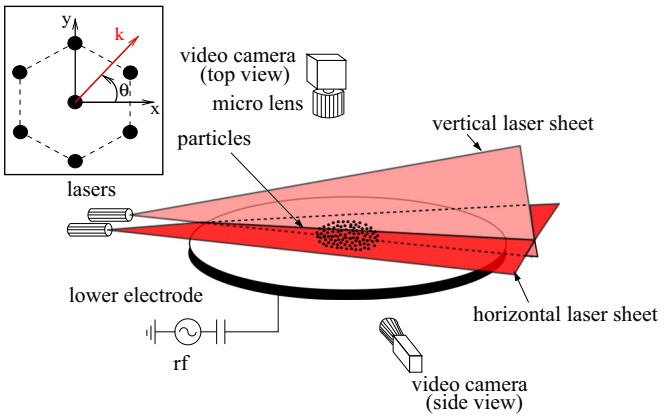

FIG. 1. (Color online) Sketch of the experimental setup. Microparticles are confined above the rf electrode and are illuminated with a horizontal laser sheet. Microparticles are recorded from top at a speed of 250 frames per second. A second vertical laser sheet illuminates the microparticle cloud allowing us to record a slice of it using a side-view camera at 103.56 fps. In the inset the elementary cell of the hexagonal lattice is depicted with the frame of reference chosen in this article.

strongly with each other, and, as has been shown previously, the hybrid mode can be a source of anomalous heating [36,37]. First experimental observations showed that at the nonlinear stage of the mode-coupling instability the crystal melts and spreads out vertically [36,39,40].

In this paper, we demonstrate experimentally that during the melting process mediated by the mode-coupling instability, the microparticle oscillations are synchronized dominantly in the direction along which the instability increment is maximal. The side-view imaging revealed that the particles exhibit both vertical and horizontal oscillatory motions at the hybrid mode frequency. The synchronization is explained by the fact that only the wave modes at the hybrid frequency have a positive growth rate while the other waves are damped. Moreover, the hybrid mode with a maximal increment is dominantly compressional.

II. EXPERIMENTAL SETUP

Mode coupling and plasma crystal melting were systematically investigated in experiments performed with a (modified) gaseous electronics conference (GEC) chamber, in a capacitively coupled rf glow discharge at 13.56 MHz (see Fig. 1). The argon pressure was between 0.4 and 1 Pa and the forward rf power was between 5 and 20 W (which corresponded to rf peak-to-peak voltage between 175 and 310 V). The plasma parameters in the bulk discharge were deduced from Langmuir probe measurements, yielding the electron temperature $T_e = 2.5$ eV and the electron density $n_e = 2 \times 10^9$ cm^{-3} at $p = 0.66$ Pa and $P = 20$ W [41]. A horizontal monolayer was formed by levitating melamine-formaldehyde particles in the plasma sheath above the lower rf electrode. Particles with a diameter of 9.19 ± 0.14 μm were used. The dust particle cloud was illuminated by two laser sheets: a vertical one and a horizontal one. The particles were imaged through a window at the top of the chamber by a Photron FASTCAM 1024 PCI camera at a speed of 250 frames per second. The horizontal coordinates x and y as well as velocity components v_x and v_y of individual particles were then extracted with subpixel resolution in each frame by using a standard particle tracking technique [42]. An additional side-view camera (Basler Ace ACA640-100GM at 103.56 fps) was used to verify that our experiments were carried out with a single layer of particles. This side-view camera was also used to study the in-plane and out-of-plane motion of the microparticles in a slice of the crystal. The diameter of the obtained crystalline structure, depending on the number of injected particles [43], was up to ~60 mm.

III. DATA PROCESSING

A. Dynamical characteristics

To explore the wave properties of the microparticle monolayer, the in-plane and out-of-plane tracking data obtained are used to compute the particle velocity fluctuation spectra. First the particle current components $V_s(\mathbf{k},t)$ introduced as

$$V_s(\mathbf{k},t) = \sum_{j=1}^{N} v_{s,j}(t) e^{-i\mathbf{k}\cdot\mathbf{s}_j(t)} \tag{1}$$

are calculated in the s direction at the time moment t, using a wave vector $\mathbf{k} = \{k_x, k_y\}$ located in the horizontal plane. Here, i is the imaginary unit, j is the particle index, $v_{s,j}(t)$ is the s projection of the jth particle velocity, $\mathbf{s}_j = \{x_j, y_j, z_j\}$ is its position, and N is the number of microparticles. Note that the x,y axes are chosen as shown in Fig. 1. Fixing the axes directions allows us to easily choose the direction of the wave propagation with respect to the lattice principal axis. A fast Fourier transform in time domain is then implemented to obtain the current fluctuation spectra. The structure factor of the crystal was also calculated from the particle positions:

$$S(\mathbf{k},t) = \frac{1}{N} \left| \sum_{j=1}^{N} e^{-i\mathbf{k}\cdot\mathbf{s}_j(t)} \right|^2 . \tag{2}$$

B. Instantaneous phase and frequency of particle oscillations

From the tracks of each traced particle, it is possible to obtain the instantaneous phases of the particle trajectories as a function of time and position. The displacements $r_j(t) = \sqrt{x_j^2(t) + y_j^2(t)}$ at hand were first filtered to remove the drift and to keep only the oscillatory parts, i.e., the "filtered" displacement $\tilde{r}_j(t)$ of the jth particle is defined as

$$\tilde{r}_j(t) = x_j(t) - \frac{1}{\Delta t} \int_{t-\Delta t/2}^{t+\Delta t/2} r_j(t')dt' \tag{3}$$

where Δt, the interval of averaging, was chosen to be the same, $\Delta t = 0.5$ s, at all $j = 1 \ldots N$. Finally the Hilbert transform was implemented to obtain the analytic signals $r_{a_j}(t)$, their instantaneous phases $\phi_j(t) = \arg[r_{a_j}(t)]$, and amplitudes $A_j(t) = |r_{a_j}|$ [44]. Maps of particle instantaneous phases were then constructed for each frame and stacked together to assemble a video [45].

The instantaneous phase computed for each particle j was used to calculate the degree of synchronization σ_j between the particle j with its closest neighbors [46],

$$\sigma_j = \frac{1}{n}\sum_{j'=1}^{n}\sigma_{jj'}, \tag{4}$$

$$\sigma_{jj'} = 1 - \frac{S_{jj'}}{S_{\max}}, \tag{5}$$

where n is the number of the closest neighbors, $S_{jj'}$ is the Shannon entropy of the cycle phase distribution between neighbors,

$$S_{jj'} = -\sum_{l=1}^{M} p_{jj'l}\ln p_{jj'l}, \quad \sum_{l=1}^{M} p_{jj'l} = 1. \tag{6}$$

Here, $p_{jj'l}$ is the fraction of the data in the lth bin in the distribution of phase differences $\phi_{jj'}(t) = \phi_j(t) - \phi_{j'}(t)(\mathrm{mod}\ 2\pi)$, $l = 1 \ldots M$, $M = 20$ is the number of bins, and $S_{\max} = \ln M$ is the maximum entropy corresponding to a uniform distribution $p_{jj'l} = M^{-1}$. The distribution of phase differences was computed with the help of a moving window procedure using the instantaneous phases $\phi_{jj'}(t)$ calculated for the 101 consecutive frames centered on the time moment t.

The synchronization index σ_j introduced by relationship (4) scales between 0 and 1. The completely synchronized (desynchronized) state corresponds to $\sigma = 1(0)$.

The time derivative of the instantaneous phase yields the instantaneous frequency $2\pi f_{\mathrm{inst}} = |\partial\phi(t)/\partial t|$.

IV. EXPERIMENTAL RESULTS

In this section, the early stage of the mode-coupling instability of a 2D complex plasma crystal triggering the frequency and phase synchronization and followed by the melting is discussed. The instability was initiated by decreasing the argon pressure from $p = 0.94$ Pa to 0.92 Pa at a fixed forward rf power $P = 12$ W.

A. Fluctuation spectra of the monolayer

The longitudinal and transverse sound speeds, respectively $C_L = (34.1 \pm 1.4)$ mm/s and $C_T = (7.9 \pm 0.3)$ mm/s, were obtained by using the low-k part of the longitudinal and transverse in-plane spectra; see Fig. 2. The interparticle separation in the center of the crystal was found to be $a = 480 \pm 10$ μm. Given the measured values of a, C_L, and C_T, and following the method proposed in Ref. [47], the charge of the dust particles $Q \simeq -18\,600e$, where e is the elementary charge, the coupling parameter $\kappa \equiv a/\lambda_D = 1.26$ and the Debye length $\lambda_D = 380$ μm were calculated. The error on the charge is about 15% and the error on κ is about 30%.

The frequency of the vertical particle oscillations (the "vertical confinement parameter") $f_v = 23 \pm 1$ Hz was extracted from the out-of-plane fluctuation spectrum (not shown here).

The hot spot at the frequency $f_{\mathrm{hyb}} = 16 \pm 1$ Hz, indicating emergence of the hybrid mode, is well pronounced in the longitudinal velocity fluctuation spectrum; see Fig. 2(a). To obtain the wave energy distribution in the $\mathbf{k}$ plane around the hybrid mode resonance frequency $f = f_{\mathrm{hyb}}$ the spectrum

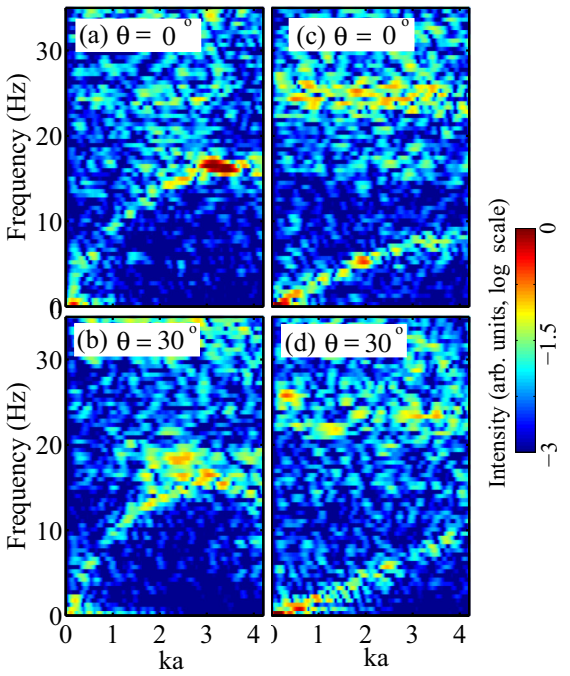

FIG. 2. (Color online) Fluctuation spectra of the in-plane particle velocity at $\theta = 0^\circ$ and $\theta = 30^\circ$: (a),(b) longitudinal, (c),(d) transverse velocity fluctuations. A bright "hot spot" at the frequency of $f_{\mathrm{hyb}} = 16 \pm 1$ Hz well seen in the spectrum (a) is worth noting.

of the in-plane velocity fluctuations was integrated over the narrow frequency band 14–18 Hz. Performing computations, the interrogation window was chosen to be a square of 400 × 400 pixels. It was thus ~35 × 35 interparticle distances giving a resolution of $\sim 0.18ka$. The resultant spectral map is shown in Fig. 3. The upper (lower) panel of Figs. 3(a) and 3(b) shows the compressional (shear) component of the velocity fluctuation.

Note that the $k_x > 0$ semiaxis corresponds to the $\theta = 0^\circ$ direction in the frame of reference introduced in Fig. 1. As predicted by the linear isotropic theory [25,37], it is the "most unstable" direction in which the instability develops. Therefore, in what follows, the $\theta = 0^\circ$ direction (as well as any other, e.g., at $\theta = \pm 60^\circ$, $\pm 120^\circ$, and 180° which are equivalent by symmetry) is referred to as the "most unstable direction."

The synchronized nonlinear state of the crystal layer oscillations happened to be highly anisotropic; see Fig. 3. For instance, inside the first Brillouin zone, the hot spot located at $\theta = 60^\circ$ is about nine times brighter than its "counterpart" located at $\theta = -120^\circ$ [Fig. 3(a)]. The hot spots expected to be at $\theta = -60^\circ$ and 120° by symmetry have astonishingly disappeared. Therefore the energy spectrum of the synchronized hybrid mode oscillations is strongly intensity and angle modulated. In this sense, the hexagonal symmetry of the crystal state is broken.

Note that "spontaneous" symmetry breaking phenomenon is a typical behavior for, e.g., driven colloids [48]. This phenomenon explains rigorously the asymmetry of the escape directions and the chirality of the defect configurations revealed by the newly nucleated dislocations in 2D complex plasma experiments [49,50].

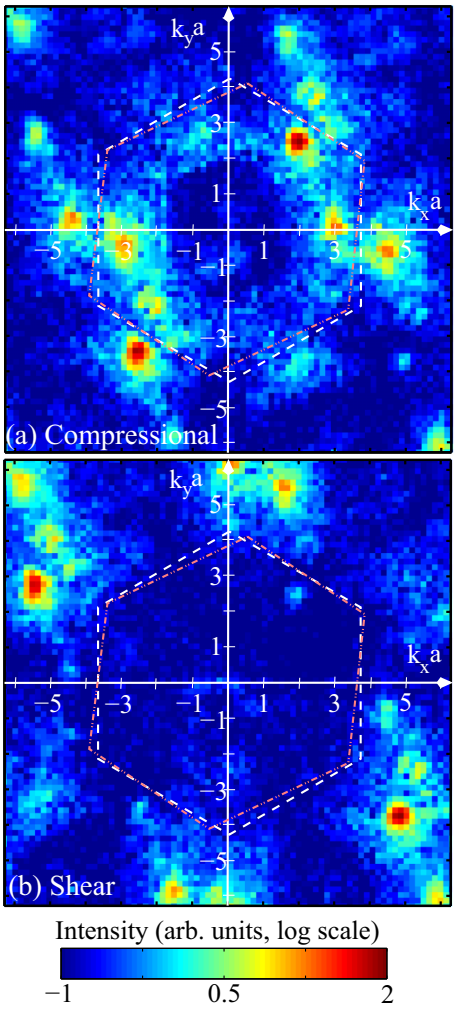

FIG. 3. (Color online) Spectrum of the particle velocity fluctuations in the $\{k_x,k_y\}$ plane integrated over the frequency in the range 14 Hz $< f <$ 18 Hz. (a) Compressional component. (b) Shear component. The white dashed lines show the border of an ideal (theoretical) first Brillouin zone. The dotted-dashed pink lines show the border of the real first Brillouin zone obtained from the time averaged structure factor $S(\mathbf{k})$. The bright hot spots located inside this zone are well recognizable in the compressional spectrum by the higher energy concentration. Their positions in the first half of the Brillouin zone are $k_1 a = 3.0 \pm 0.2$, $\theta_1 = (3 \pm 5)^\circ$, and $k_2 a = 3.2 \pm 0.3$, $\theta_2 = (60 \pm 7)^\circ$. Note an asymmetry effect: the 60° hot spot is certainly brighter and no hot spot is observed at −60°. A large-scale inhomogeneity of the monolayer is most probably responsible for all of the observed anisotropy.

As can be seen in Fig. 3(a), the hot spot positioned, for instance, along a $k_x > 0$ semiaxis is located in the **k** map at $k_x = k_{\mathrm{hyb}}$, which is close to the very right border of the first Brillouin zone k_{Br}, still distinguishably well separated from it:

$$k_{Br} a = 2\pi/\sqrt{3} > k_{\mathrm{hyb}} a \simeq \pi,\ (k_{Br} - k_{\mathrm{hyb}})/k_{\mathrm{hyb}} \simeq 15\%.$$

The accuracy of given measurements, around 5–10%, allows us to certainly state this.

It should also be noted that in Fig. 3(b), one can see a slight excitation of shear waves in the direction of main instability (especially at 60°). Since the theory predicts that the hybrid mode does not have a shear component, this is quite surprising. However, the intensity of the shear component is around two orders of magnitude less than the compressional component. This probably originates in the nonlinearity of the coupled waves.

B. Partial synchronization

The evolution of the cumulative probability $p(f_{\mathrm{hyb}})$ to find the instantaneous frequency inside the frequency band 14–18 Hz around the hybrid resonance $f_{\mathrm{inst}} \sim f_{\mathrm{hyb}}$ is presented in Fig. 4. At start ($t < 0.5$ s), the frequency synchronization probability is low. Then, as the mode-coupling instability sets in, the probability gradually increases as more and more particles get locked at the hybrid frequency. Between $t = 2.5$ s and $t = 3$ s, there appears a significant fraction of the particles that oscillate at the hybrid frequency, indicating emergence of the partial frequency synchronization state. When the crystalline suspension melts (at $t > 3$ s), the cumulative probability drops down stepwise to the lowest level ∼0.05 indicating no frequency synchronization, and, hence, no mode coupling. Only the central parts of the monolayer were involved in calculations, half in size compared to those used to assemble the phase distribution maps shown on top in Fig. 4.

Note that sharp change in the phase locking probability is typical for the dynamical phase transitions, e.g., for Josephson junction arrays [14].

The pair correlation functions shown in the inset in the bottom panel of Fig. 4 demonstrate partial degradation of the crystalline order during the transitions between the synchronized and desynchronized states.

The snapshots of the instantaneous phase variation during the mode-coupling instability are presented in the top panels of Fig. 4. The phase locking proceeds as follows:

(i) At the beginning at $t < 1$ s, no recognizable synchronization pattern can be extracted and the instantaneous phases appear to be randomly distributed over the crystal layer.

(ii) Starting from $t \simeq 1.3$ s (first map shown on top in Fig. 4), short rows of in-phase oscillating particles can be detected in the central part of the crystal, indicating that partial synchronization of the particle motions takes place.

(iii) With time passed, at $t = 2.16$ s, rows of the in-phase oscillating particles elongate as more particles become involved in synchronization (second map shown on top in Fig. 4). It is worth mentioning that neighboring rows of the synchronically oscillating particles are moving almost in antiphase (i.e., having a phase difference $\Delta\phi \simeq \pi$). Note also that the motion of the synchronically moving particles is strongly "polarised" in the $\theta = 60^\circ$ direction.

(iv) Later on, at $t = 2.94$ s (third map shown on top in Fig. 4), two types of the phase alignment, one oblique (corresponding to the wave propagation angle $\theta \simeq 60^\circ$) and another almost vertical (corresponding to the wave propagation angle $\theta \simeq 0^\circ$), are clearly seen. Apparently, they correspond to two equivalent directions, by symmetry, in the crystal. The synchronization effect can also be well identified through increase in the mean value of the synchronization index $\langle\sigma\rangle$ (averaged over particles). The averaged Shannon entropy of the cental part of the crystal (blue line in bottom panel of

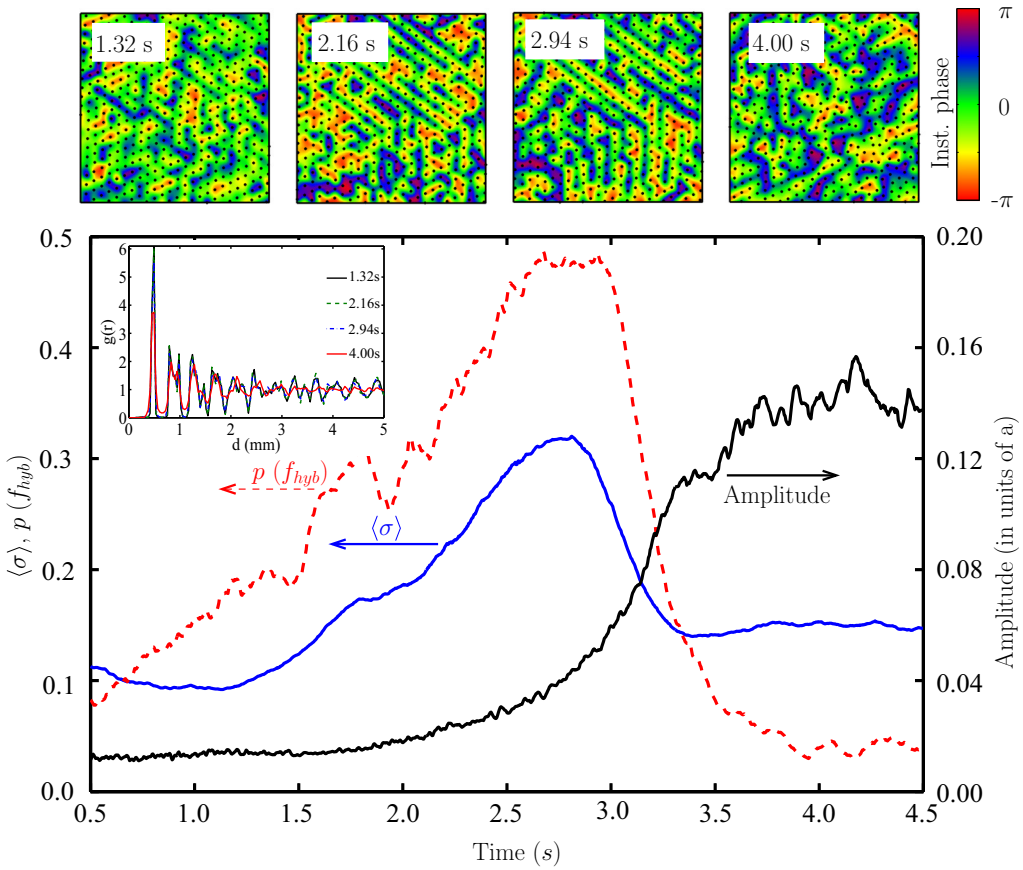

FIG. 4. (Color online) (top) Consecutive snapshots (a 300×300-pixel area of the original video) indicating the instantaneous phase distribution for desynchronized phase states (the very left and right images, $t = 1.32$ s and $t = 4.00$ s), and during the synchronization state (two middle images, $t = 2.16$ s and $t = 2.94$ s). Black dots show the position of the particles. (bottom) Evolution of the cumulative probability $p(f_{\rm hyb})$ (red dashed curve) to find a particle with an instantaneous frequency in the band 14 Hz $< f <$ 18 Hz around $f_{\rm hyb}$, the mean value of the synchronization index $\langle\sigma\rangle$ (averaged over particles, solid blue curve) and the averaged instantaneous amplitude of the particle oscillations (solid black curve). Performing the averaging, about 150 particle tracks at the center of the crystal (a 145×145-pixel area of the original video) were taken into account. The inset shows the radial pair correlation functions taken at the indicated time moments.

Fig. 4) grows almost linearly during the first 1.5 s, and shows a maximum at the most synchronized state.

(v) The lifetime of the synchronized state is about $\Delta t = 1$ s in our conditions. It is important to emphasize that the synchronization pattern self-assembles (and then disappears after a while) almost simultaneously in the phase-locking and frequency-locking processes. It is also worth noting that the degree of phase synchronization is maximal when the probability to find the frequency locked in the vicinity of the hybrid resonance is also maximal; see blue and red curves in Fig. 4. Notice that phase and frequency synchronization starts at small but finite amplitude of particle oscillations. It can be clearly seen in Fig. 4 that the amplitude of the particle oscillations (solid black line) is nearly exponentially growing during the synchronization period. It corresponds fairly well to the theoretical expectations [37].

(vi) The pair correlation function $g(r)$ (see the inset in Fig. 4) shows that the crystalline structure is preserved for a surprisingly long time. Nonetheless, at $t > 3$ s, when the oscillations become too intense, the synchronization degree goes down indicating that the phase locking no longer takes place and the particle oscillations desynchronize (see fourth map shown on top of Fig. 4). The crystal melts and the partial synchronization state is lost.

C. Tracks of synchronically oscillating particles

To study in detail the out-of-plane particle vibrations, the mode-coupling induced crystal melting process was recorded from the side of the monolayer at a frame rate of 103.56 fps (see Fig. 1). The trajectories of two neighboring particles were traced and extracted from the recorded sequence of the side-view images. These trajectories are presented in Fig. 5. The time averaged values were subtracted from the actual particle positions in order to emphasize the oscillatory part of the particle movements. Both particles exhibit an oscillatory motion at the hybrid frequency $f_{\rm hyb} \simeq 16.5 \pm 0.8$ Hz. Their motion consists of the vertical ("out-of-plane") and horizontal ("in-plane") approximately equally energized components. This fact is in a fairly good agreement with that theoretically expected [23,25,37,51]. It is also worth noting that the trajectories shown in Fig. 5, belonging to the neighboring

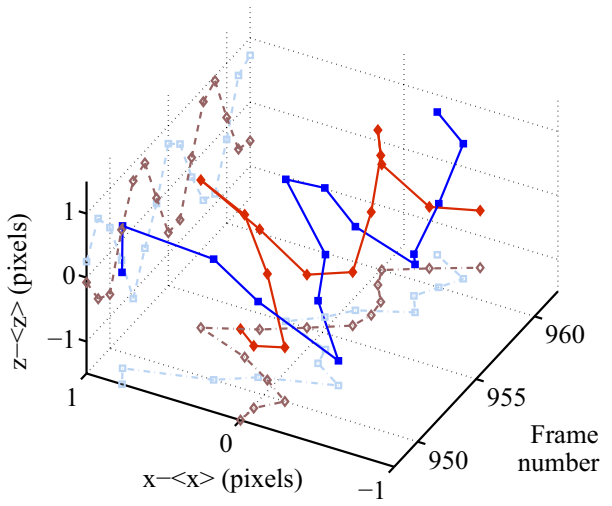

FIG. 5. (Color online) Trajectories of two neighbor particles [red (plain diamond symbols) and blue (plain square symbols) plain lines] exhibiting a periodic motion at the hybrid frequency $\simeq 16.5 \pm 0.8$ Hz in both the vertical and horizontal directions. The dashed light-blue (opened square symbols) and light-red (opened diamond symbols) lines are the projection on the (x,t) and (z,t) planes.

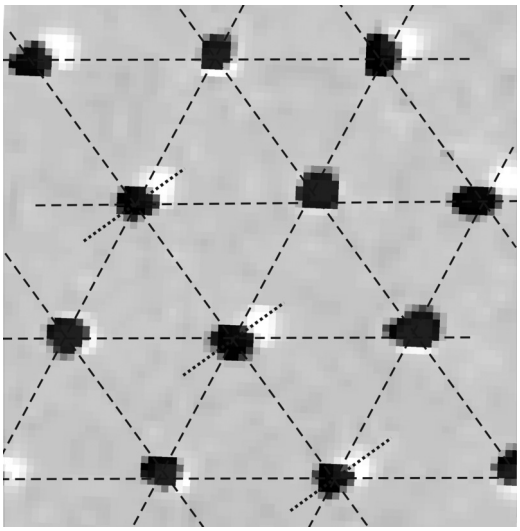

FIG. 6. Two superposed images of the lattice layer separated in time by a half period ($\Delta t \simeq 0.032$ s). The absolute time moment, $t \simeq 2.7$ s, was taken close to the maximum of the synchronization index; see Fig. 4. The white and black dots represent the particle positions. The mean interparticle separation in the chosen region is $\langle a \rangle = 470 \pm 16$ μm. Three sets of parallel dashed lines are shown to guide the eye. The stacked images were shifted along the main deformation direction to graphically demonstrate the character of the particle vibrations. The main deformation direction is as the dotted lines indicate. Note that in this direction the lattice is about 7–9% more compact. Importantly, the distance between the in-phase oscillating rows of particles is kept nearly constant.

chains of particles, present antiphase oscillations in pretty good agreement with that shown in Fig. 4. (The measured phase difference is in the z direction, $\langle \Delta\phi_z \rangle = (1.03 \pm 0.10)\pi$, and in the x direction, $\langle \Delta\phi_x \rangle = (1.49 \pm 0.70)\pi$. The large error in the last case can be explained by the fact that the laser sheet was not properly aligned along the crystal main axis.)

The interpenetrating antiphase oscillating "sublattices" is the general pattern most closely explaining synchronization in a 2D plasma crystal; see Fig. 6. In this sense, the synchronized state of a 2D complex plasma obeys the common well-established rule stated in Ref. [1]: "symmetry breaking governs the ways that coupled oscillators can behave."

V. DISCUSSION AND CONCLUSION

The equation of motion of each particle in an infinite quasi-2D crystal can be written as

$$m\frac{d^2\mathbf{r}_j}{dt^2} = -m\nu\frac{d\mathbf{r}_j}{dt} - m\Omega_{\rm conf}^2(z_j - z_{eq})\mathbf{e}_z + \sum_{j'\neq j}\mathbf{F}_{jj'} + \mathbf{L}_j, \tag{7}$$

where m is the mass of the microparticles, $\mathbf{r}_j = \{x_j, y_j, z_j\}$ is the coordinate of the jth particle, z_{eq} is the vertical equilibrium coordinate same for all particles (the particles are assumed to be monodisperse), $\mathbf{e}_z$ is the unit vector in the vertical z direction, ν is the neutral gas drag coefficient, $\Omega_{\rm conf} = 2\pi f_v$ is the confinement parameter of the vertical confinement potential well (here assumed to be parabolic). The Langevin force is defined as

$$\langle \mathbf{L}_j(t) \rangle = \mathbf{0}, \quad \langle \mathbf{L}_j(t+\tau)\mathbf{L}_k(t) \rangle = 2\nu m T \delta_{jk}\delta(\tau),$$

where T is the temperature of the background gas (thermostat) in energy units [here, δ_{jk} is the Kronecker δ and $\delta(\tau)$ is the Dirac δ function]. $\mathbf{F}_{jj'} = \mathbf{F}_{jj'}^{(Y)} + \mathbf{F}_{jj'}^{(w)}$ is the interaction force between the two particles. This force consists of the screened Coulomb interaction

$$\mathbf{F}_{jj'}^{(Y)} = Q^2\frac{\mathbf{r}_{jj'}}{r_{jj'}^3}\left(1 + \frac{r_{jj'}}{\lambda_D}\right)\exp\left(-\frac{r_{jj'}}{\lambda_D}\right)$$

and the ion-wake-mediated interaction force $\mathbf{F}_{jj'}^{(w)}$, introduced, e.g., in Ref. [23]. In [23], by using a simple model, in which the ion wake was modelled by a pointlike positive charge located at a fixed distance below the particle, it was shown that the longitudinal in-plane and transverse out-of-plane wave modes $\omega(\mathbf{k})$ merge at a certain critical value of $\Omega_{\rm conf}$. Strongly coupled vertical and horizontal particle movements result in the formation of the hybrid mode. The hybrid mode emergence is characterized by a positive growth rate, which can trigger the mode-coupling instability (see Refs. [23,25,37] for details). Calculations done for a more refined wake potential model (performed in Refs. [34,35]) do not change the main characteristics of the mode coupling. According to [23,25,37,51], the hybrid mode has both in-plane longitudinal and out-of-plane transverse components, which are equally strong. In Ref. [25], it is also shown that the coupling occurs close to the boundary of the first Brillouin zone. All these predictions are well in line with our observation results.

As can be seen in Figs. 2 and 3, most of the spectral energy of fluctuations is concentrated in the hybrid modes excited in the most unstable direction (i.e., for $\theta = 0^\circ$ in our adopted frame of reference). Consequently, the particle motion surveyed from the top view should be mainly seen as

oscillations around the equilibrium positions, occurring in this direction at the hybrid frequency. Figure 5 confirms that the hybrid mode has both the vertical and horizontal components. In Fig. 4, it can be seen that the entire rows comprising 10–20 particles have the same instantaneous phase, especially at the latest stage of the instability (before the crystal melts). This effective "one-dimensionalization" by phase and frequency locking deeply affects the synchronization pattern. As already mentioned in the previous section, it can also be seen in Fig. 4 that every two consecutive rows containing "in-phase" moving particles oscillate almost in antiphase with each other. The latter can be explained by the fact that the hybrid mode with synchronized particle motion has a wave number $k \simeq k_{\mathrm{hyb}}$ closely obeying the relationship $ka \simeq k_{\mathrm{hyb}}a \simeq \pi$. Since the wave oscillations of the particle j are proportional to $e^{i\mathbf{k}\cdot\mathbf{r}_j}$, we immediately conclude that for such k the motion of neighboring particles should indeed be almost antiphase; see also Ref. [23].

When the instability is triggered, only the oscillations associated with the hybrid mode can surpass the damping, while all other wave modes tend to equilibrium with the surrounding plasma. Consequently, the kinetic energy is accumulated in the hybrid mode and the amplitude of the corresponding oscillations grows exponentially, hiding any motion related to other modes sustained in the crystal. This effect explains why the particle motion gets synchronized with time in the direction of the main instability, and the amplitude exhibits an exponential growth (see Fig. 4). Moreover, it is easy to show that, by making a second order Taylor expansion of the force between two neighbor particles, a coupling between the particle phases of both the in-plane motions and out-of-plane motions exists (i.e., terms in $x_j z_{j+1}$, $z_j x_{j+1}$, $x_j x_{j+1}$, and $z_j z_{j+1}$, which make a dependence of the force exerted on the jth particle on the horizontal and vertical phases of the $(j+1)$th particle automatically appear). It is well known that oscillators with any phase-dependent interaction can evolve until their phases are (partially) synchronized [12].

Since the hybrid mode with maximal increment has only a very weak shear in-plane component (Fig. 3), it naturally occurs that rows of particles which belong to equivalent elementary cells must have synchronized motion (two cells are equivalent when the translation necessary to pass from one to the other results in a phase shift such that $\Delta\Phi \mod 2\pi = 0$).

When the amplitude of motion is too large, the monolayer becomes disordered and the synchronization power naturally vanishes.

In Fig. 4, it can be seen that only two of three possible equivalent by symmetry directions were excited. We believe that the third direction has a higher excitation level due to inhomogeneity of the horizontal confinement, leading to inhomogeneities in the density of the crystal, breaking the symmetry of synchronization pattern.

It is worth noting that despite synchronization in plasma crystals was so far never systematically studied, traces of the synchronized particle motion could be also detected in Ref. [36] (especially at a low discharge power and low gas pressure). Interestingly, when the crystal layer is not circular but elliptical, the synchronization pattern seems to be preferentially observed in the direction of the minor axis of the ellipse.

Thus, we have shown that during the mode-coupling induced melting, the formation of the unstable hybrid mode leads to the partial synchronization of the particle motion in the direction of the main instability. It was evidenced by analysis of the instantaneous phase, instantaneous frequency, and synchronization index (Shannon entropy). The frequency and the phase synchronization processes could be explained by the fact that only wave modes at the hybrid frequency have a positive growth rate while the other modes are well attenuated by the damping.

ACKNOWLEDGMENTS

This work was supported by the European Research Council under the European Union's Seventh Framework Programme (FP7/2007-2013), ERC Grant Agreement No. 267499, and by the French-German PHC PROCOPE program (Project No. 28444XH/55926142). The authors would like to thank Dr. O. Agullo, Dr. D. Escande for fruitful discussions, and Dipl. Ing. M. Zhdanova for help.

[1] S. H. Strogatz and I. Stewart, Sci. Am. **269**(6), 102 (1993).
[2] M. Bennett, M. F. Schatz, H. Rockwood, and K. Wiesenfeld, Proc. R. Soc. London Ser. A **458**, 563 (2002).
[3] N. Wiener, *Cybernetics; or Control and Communication in the Animal and the Machine* (Wiley, New York, 1948).
[4] A. T. Winfree, J. Theor. Biol. **16**, 15 (1967).
[5] S. H. Strogatz, Nature (London) **410**, 268 (2001).
[6] S. H. Strogatz, *Sync: The Emerging Science of Spontaneous Order* (Hyperion, New York, 2003).
[7] J. A. Freund, L. Schimansky-Geier, and P. Hänggi, Chaos **13**, 225 (2003).
[8] A. Arenas, A. Díaz-Guilera, J. Kurths, Y. Moreno, and C. Zhou, Phys. Rep. **469**, 93 (2008).
[9] H. G. Winful and L. Rahman, Phys. Rev. Lett. **65**, 1575 (1990).
[10] T. Heil, I. Fischer, W. Elsässer, J. Mulet, and C. R. Mirasso, Phys. Rev. Lett. **86**, 795 (2001).
[11] E. A. Rogers-Dakin, J. García-Ojalvo, D. J. DeShazer, and R. Roy, Phys. Rev. E **73**, 045201 (2006).
[12] Y. Kuramoto, *Chemical Oscillations, Waves, and Turbulence* (Springer-Verlag, New York, 1984).
[13] R. Mirollo and S. Strogatz, SIAM J. Appl. Math. **50**, 1645 (1990).
[14] K. Wiesenfeld, Physica B: Condens. Matter **222**, 315 (1996).
[15] G. E. Morfill and A. V. Ivlev, Rev. Mod. Phys. **81**, 1353 (2009).
[16] D. Samsonov, A. V. Ivlev, G. E. Morfill, and J. Goree, Phys. Rev. E **63**, 025401 (2001).
[17] S. Nunomura, D. Samsonov, and J. Goree, Phys. Rev. Lett. **84**, 5141 (2000).
[18] V. A. Schweigert, I. V. Schweigert, V. Nosenko, and J. Goree, Phys. Plasmas **9**, 4465 (2002).
[19] D. Samsonov, S. Zhdanov, and G. Morfill, Phys. Rev. E **71**, 026410 (2005).

[20] L. Couëdel, D. Samsonov, C. Durniak, S. Zhdanov, H. M. Thomas, G. E. Morfill, and C. Arnas, Phys. Rev. Lett. **109**, 175001 (2012).
[21] S. V. Vladimirov, P. V. Shevchenko, and N. F. Cramer, Phys. Rev. E **56**, R74 (1997).
[22] D. H. E. Dubin, Phys. Plasmas **7**, 3895 (2000).
[23] A. V. Ivlev and G. Morfill, Phys. Rev. E **63**, 016409 (2000).
[24] K. Qiao and T. W. Hyde, Phys. Rev. E **68**, 046403 (2003).
[25] S. K. Zhdanov, A. V. Ivlev, and G. E. Morfill, Phys. Plasmas **16**, 083706 (2009).
[26] O. Ishihara and S. V. Vladimirov, Phys. Plasmas **4**, 69 (1997).
[27] M. Lampe, G. Joyce, G. Ganguli, and V. Gavrishchaka, Phys. Plasmas **7**, 3851 (2000).
[28] A. Melzer, V. A. Schweigert, and A. Piel, Phys. Scr. **61**, 494 (2000).
[29] L.-J. Hou, Y.-N. Wang, and Z. L. Mišković, Phys. Rev. E **64**, 046406 (2001).
[30] S. V. Vladimirov, S. A. Maiorov, and O. Ishihara, Phys. Plasmas **10**, 3867 (2003).
[31] A. Samarian, S. Vladimirov, and B. James, JETP Lett. **82**, 758 (2005).
[32] W. J. Miloch, Plasma Phys. Controlled Fusion **52**, 124004 (2010).
[33] R. Kompaneets, U. Konopka, A. V. Ivlev, V. Tsytovich, and G. Morfill, Phys. Plasmas **14**, 052108 (2007).
[34] T. B. Röcker, A. V. Ivlev, R. Kompaneets, and G. E. Morfill, Phys. Plasmas **19**, 033708 (2012).
[35] T. B. Röcker, S. K. Zhdanov, A. V. Ivlev, M. Lampe, G. Joyce, and G. E. Morfill, Phys. Plasmas **19**, 073708 (2012).
[36] L. Couëdel, V. Nosenko, A. V. Ivlev, S. K. Zhdanov, H. M. Thomas, and G. E. Morfill, Phys. Rev. Lett. **104**, 195001 (2010).
[37] L. Couëdel, S. K. Zhdanov, A. V. Ivlev, V. Nosenko, H. M. Thomas, and G. E. Morfill, Phys. Plasmas **18**, 083707 (2011).
[38] J. A. Acebrón, L. L. Bonilla, C. J. Pérez Vicente, F. Ritort, and R. Spigler, Rev. Mod. Phys. **77**, 137 (2005).
[39] A. V. Ivlev, U. Konopka, G. Morfill, and G. Joyce, Phys. Rev. E **68**, 026405 (2003).
[40] J. D. Williams, E. Thomas, L. Couëdel, A. V. Ivlev, S. K. Zhdanov, V. Nosenko, H. M. Thomas, and G. E. Morfill, Phys. Rev. E **86**, 046401 (2012).
[41] V. Nosenko, A. V. Ivlev, S. K. Zhdanov, M. Fink, and G. E. Morfill, Phys. Plasmas **16**, 083708 (2009).
[42] S. S. Rogers, T. A. Waigh, X. Zhao, and J. R. Lu, Phys. Biol. **4**, 220 (2007).
[43] We explored a range of the particle numbers from 1000 to 20 000.
[44] K. O. Menzel, O. Arp, and A. Piel, Phys. Rev. E **83**, 016402 (2011).
[45] See Supplemental Material at http://link.aps.org/supplemental/10.1103/PhysRevE.89.053108 for a video showing the evolution of the instantaneous phase distribution.
[46] R. Toth and A. F. Taylor, J. Chem. Phys. **125**, 224708 (2006).
[47] S. Nunomura, J. Goree, S. Hu, X. Wang, A. Bhattacharjee, and K. Avinash, Phys. Rev. Lett. **89**, 035001 (2002).
[48] C. Reichhardt and C. J. O. Reichhardt, Europhys. Lett. **68**, 303 (2004).
[49] V. Nosenko, S. Zhdanov, and G. Morfill, Philos. Mag. **88**, 3747 (2008).
[50] S. K. Zhdanov, M. H. Thoma, C. A. Knapek, and G. E. Morfill, New J. Phys. **14**, 023030 (2012).
[51] T. B. Röcker, A. V. Ivlev, S. K. Zhdanov, and G. E. Morfill, Phys. Rev. E **89**, 013104 (2014).